Late Quaternary Dust, Loess and Desert Dynamics in Upwind Areas of the Chinese Loess Plateau

Mingrui Qiang[1], Thomas Stevens[2], Guoqiang Li[3], Ling Hu[3], Xiaowei Wang[3], Wenzhe Lang[3], and Jie Chen[1]

[1]South China Normal University
[2]Uppsala University
[3]Lanzhou University

November 23, 2022

Abstract

As a key global climate and dust archive, the nature of Chinese loess deposition remains debated. We investigate chronostratigraphic variability of eolian deposits in upwind regions of the modern Chinese Loess Plateau (CLP) and reconstruct dust dynamics that potentially affects loess deposition downwind. The strata consist of alternating layers of typical loess, well-sorted sand, and sandy loess, with obvious unconformities occurring at the transitions from loess to sand. We suggest that pre-existing typical loess was eroded by wind, providing homogeneous dust for loess on the CLP. The interbedded well-sorted sand and loess suggest that proximal deserts have greatly expanded and contracted repeatedly, strongly affecting dust emission and transport and thus leading to significant changes in dust accumulation rates on the CLP. Our results suggest active dust processes in upwind regions of the CLP have major implications for using loess sequences to deduce climate and dust changes.

Late Quaternary Dust, Loess and Desert Dynamics in Upwind Areas of the Chinese Loess Plateau

Mingrui Qiang[1,2], Thomas Stevens[3], Guoqiang Li[2], Ling Hu[2], Xiaowei Wang[2], Wenzhe Lang[2], and Jie Chen[1]

[1]School of Geography, South China Normal University, Guangzhou 510631, China, [2]MOE Key Laboratory of Western China's Environmental Systems, Lanzhou University, Lanzhou 730000, China, [3]Department of Earth Sciences, Uppsala University, Villavägen 16, Uppsala 75236, Sweden

Corresponding to: Mingrui Qiang
Email: mrqiang@scnu.edu.cn

Key Points:

- Typical loess has been deposited in areas upwind of the present Chinese Loess Plateau and then partially eroded by wind
- Entrained loess material provides a source of homogeneous dust for leeward loess, actually complicating interpretation of routine proxies
- Episodic expansion and contraction of proximal deserts strongly affected dust emission in source areas and thus dust deposition leeward

Abstract

As a key global climate and dust archive, the nature of Chinese loess deposition remains debated. We investigate chronostratigraphic variability of eolian deposits in upwind regions of the modern Chinese Loess Plateau (CLP) and reconstruct dust dynamics that potentially affects loess deposition downwind. The strata consist of alternating layers of typical loess, well-sorted sand, and sandy loess, with obvious unconformities occurring at the transitions from loess to sand. We suggest that pre-existing typical loess was eroded by wind, providing homogeneous dust for loess on the CLP. The interbedded well-sorted sand and loess suggest that proximal deserts have greatly expanded and contracted repeatedly, strongly affecting dust emission and transport and thus leading to significant changes in dust accumulation rates on the CLP. Our results suggest active dust processes in upwind regions of the CLP have major implications for using loess sequences to deduce climate and dust changes.

Plain Language Summary

Loess material is mainly composed of mineral dust, carried by wind from arid regions and then settled downwind. Due to their large area and huge thickness, the Chinese loess deposits are one of most important records for understanding the history of global climate and atmospheric dust changes. In order to link the physical properties of loess to climatic changes, and to use records of dust accumulation in loess to infer past atmospheric dustiness, we need to know how loess material is generated and transported, and what can affect this. We found that alternating layers of typical loess and desert

sand occur in regions upwind of the Chinese Loess Plateau, today dominated by sandy desert landscapes. The replacement of loess by sand in these areas tells that pre-existing loess has been eroded and transported downwind to the Chinese Loess Plateau. This implies that the accumulation and properties of loess on the Chinese Loess Plateau are heavily affected by this process, and not only a function of drought in source areas, as previously believed. This work provides an important step in uncovering the nature of loess accumulation and using it to understand past changes in climate.

1. Introduction

As one of the world's key climate archives, Chinese loess deposits have been widely used to decipher changes in continental environments and atmospheric circulation on various timescales (e.g., Hovan et al., 1989; Liu & Ding, 1998; Guo et al., 2002; Sun et al., 2012; Licht et al., 2014). However, the nature of loess deposition and the processes that could affect this have generally not been investigated in detail within loess-based climatic reconstructions, with most studies assuming largely consistent dust emission, transport and deposition for given intervals.

Chinese loess deposits are mainly derived from the arid and semiarid regions of China, constituting source proximal dust deposits of the Asian eolian system (Rea, 1994; Biscaye et al., 1997; Uno et al., 2009; Shao et al., 2011). Thus, loess deposition must be affected by a complex range of surface processes and local influences (Stevens et al., 2006), including aridity in source areas, dust transport capacity, and changes in the scope of source areas and hence in materials supplying dust. Recently, Kapp et al. (2015)

mapped the landforms of the Ordos Basin and the northern Chinese Loess Plateau (CLP), and concluded that thick loess may have been previously distributed in areas further to the north and west than the present CLP, but was subsequently eroded by winds, supplying homogeneous dust to younger loess deposits leeward. This work emphasized that loess in upwind regions from the current CLP would be a previously unrecognized dust source, suggesting a process of “eolian cannibalism” of previously deposited loess. A large amount of zircon U-Pb data from loess and different potential dust source deposits suggest that a substantial portion of interglacial dust is recycled from older glacial loess (Licht et al., 2016), implying reworking of older loess deposits by wind. Furthermore, multiple erosional hiatuses during the past 300 ka, recorded by loess deposits at Jingbian, provide independent evidence that supports the hypothesis of loess cannibalization from CLP marginal areas (Stevens et al., 2018). These findings therefore call for urgent reassessments of changes in potential sources of Chinese loess, of accepted interpretations of climatic proxies applied to loess deposits, such as sedimentation rate and grain size, of Quaternary dust dynamics in this globally important dust emission region, and even exactly how the Chinese loess time series can represent large-scale climatic changes. To test these findings requires analysis of the complex sedimentary system source to sink, including understudied aeolian sediment that lies between the main CLP and the main source areas. However, to date, beyond a few well dated sites (Xu et al., 2018), there is still a lack of chronostratigraphic evidence over the age and geographical extent of loess upwind of the main CLP. Potential previously active depositional regions are currently dominated by desert landscapes and subjected to intense eolian erosion. This means the potential for pre-existing loess to act as a dust source and for the influence of proximal desert activity on loess accumulation on the CLP remains unclear.

In this study, we investigate chronostratigraphic variability and changes in grain size of eolian deposits outside the boundary of the modern CLP, aiming to understand (1) the possible distribution of pre-existing loess areas in upwind regions of the CLP, (2) the influence of dust entrained from pre-existing loess on the CLP loess, and (3) the evolution of proximal deserts during the Late Quaternary and the potential impact on loess sequences. Our results provide insights into dust dynamics in regions upwind of the CLP, which are crucial for understanding environmental and climatic changes recorded by loess sequences from the CLP and in constraining the specific dust source areas of one of the most important dust source regions in the world.

2. Study Sites and Methods

As an intermediate product of airborne transport, eolian deposits between proximal deserts and the CLP share features of both source materials and loess deposits (Qiang et al., 2010), and thus are a crucial link in deciphering dust dynamics between source areas to dust depositional regions. Three outcrop sections of eolian deposits at two sites northwest of the modern CLP were selected for detailed investigation. Two sections in the Xiangshan Mountains (sections XS-A and XS-B; 37º20′8″N, 105º13′36″E) are on a rocky platform of tectonic origin along the central northern slopes of the range, which is separated from the Tengger Desert by the Yellow River (Figures 1a and S1). The site is at an altitude of 1645 m a.s.l. and is ~500 m higher than the Yellow River. The mean annual temperature and precipitation of the area were 9.7 °C and 187 mm respectively during 1965–1980 (Qiang et al., 2010), and the maximum wind speed in spring was 29.1 m s^{-1}. The Kajia section (KJ; 35º33′27.6″N, 100º58′44.3″E) is located at the southeastern margin of the Mugetan Sandy Land in the Gonghe Basin on the NE edge of the Qinghai-Tibetan plateau, at an altitude of 3280 m a.s.l. The mean annual temperature and rainfall were 2.3 °C and 403 mm over the past 50 years.

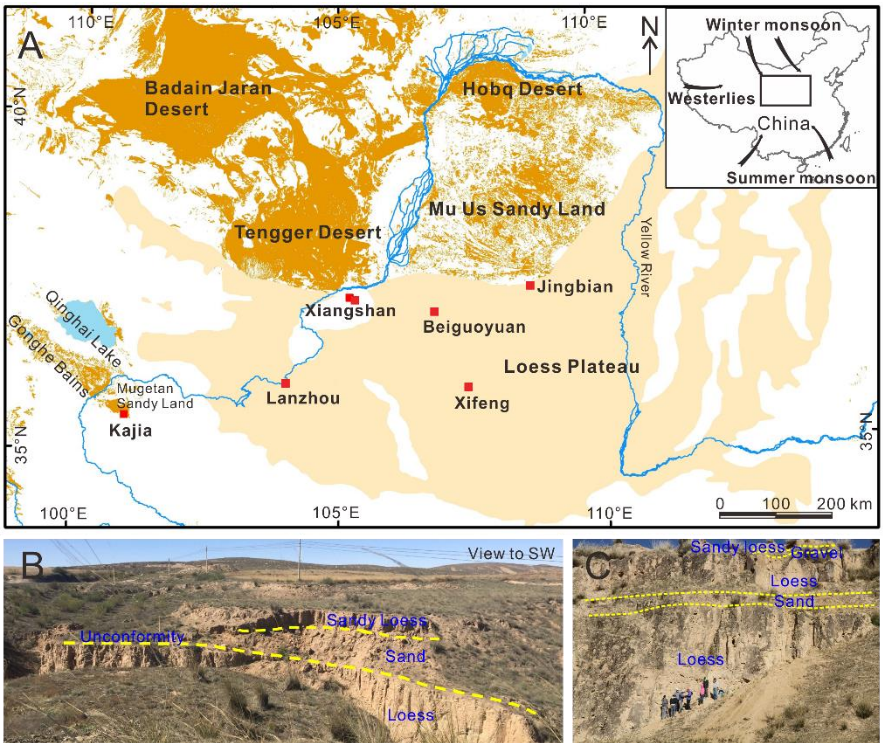

Figure 1. Physical environments along the boundary between proximal deserts and the Chinese Loess Plateau (a). Locations of the studied sites and the referenced loess sites are shown by red solid squares. Photographs of sections XS-A (b) and KJ (c). Dashed lines indicate stratigraphic boundaries.

Bulk samples were collected from the sections at intervals of 2–10 cm. Sediment grain-size distributions were measured using a laser particle analyzer (see the supporting information). Considering that the quartz optically stimulated luminescence (OSL) signal is likely to be saturated for pre Late Quaternary strata, the chronologies of sections XS-B and KJ and the age of sample XS-A-07 are determined using K-feldspar post-IR Infra-Red Stimulated Luminescence (IRSL) techniques (Buylaert et al., 2012, 2015) (see the supporting information; Table S1). A pIRIR dating protocol, utilizing a post IR IRSL signal stimulated at 290°C, was used for K-feldspar equivalent dose determination of coarse-grained K-feldspar (60/90–125 μm). Dose recovery tests were also conducted on sunlight bleached samples XS-B-01 and XS-A-07 to further check the suitability of the pIRIR dating protocol. Concentrations of U, Th, and K were measured by neutron activation analysis to determine the external sediment dose rate of quartz and K-feldspar samples. Together with previously published quartz OSL ages (Qiang et al., 2010) and an unpublished quartz OSL age from section XS-A (sample XS-A-04) using the same methodology, 21 luminescence dates are presented here (Table S1). As a result of saturated or near saturated signals (D_e value exceeding c. 700 Gy, the average $2D_0$ value for these samples), the K-feldspar pIRIR ages from the lower parts of sections XS-B and KJ are taken as minimum age estimates.

3. Results and Discussion

3.1. Stratigraphy

The stratigraphic units of the eolian deposits are easily identified in the field and are mainly composed of loess, eolian sand, and sandy loess/paleosol in the upper parts of the sequences (Figure 2a). Eolian sand is homogenous and yellowish in color, with a loose structure. Loess is homogenous, finer and denser compared to the eolian sand,

and has no visible signs of pedogenic alteration. Sandy loess contains several weakly-developed paleosols characterized by a massive and dense structure, abundant apertures, and secondary filamentous carbonates. These features make the paleosols more resistant to wind erosion compared to sand layers, resulting in the formation of loess/paleosol cliffs due to sand collapse (Figure 1b). In section KJ, eolian deposition was interrupted by fluvial processes at a depth of 250 cm, producing a layer of gravels and overbank silty sand deposits (Figures 1c and 2a).

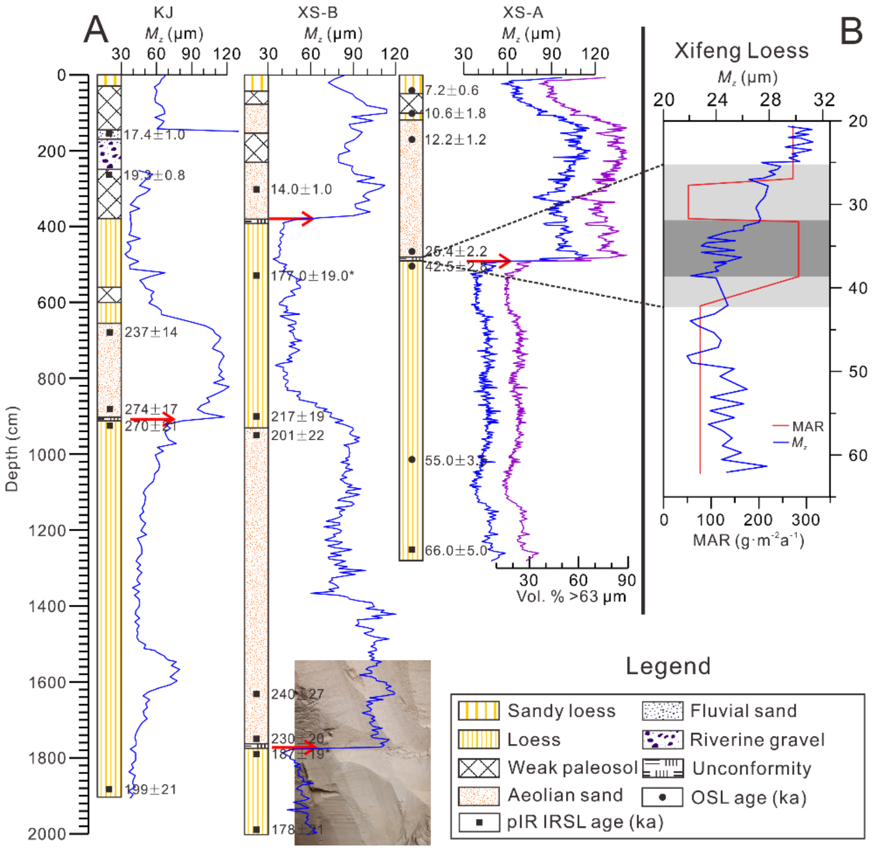

Figure 2. Stratigraphy and variations in mean grain-size (M_z) of eolian deposits in sections XS-A, XS-B and KJ (a). For section XS-A, changes in the sand fraction (>63 μm) are shown by a purple line. Red arrows indicate abrupt changes in M_z, representing unconformities. Photograph shows an unconformity between loess and eolian sand. Changes in mass accumulation rate (MAR) and M_z of the Xifeng loess during the last glacial (Stevens et al., 2016) (b), which are compared with an unconformity occurring

between 42.5 and 25.4 ka in section XS-A. The inconsistency between MAR and M_z from 39 to 32 ka is highlighted in darker gray.

The alternating strata are also clearly reflected by variations in the grain-size distributions of the samples. The loess is dominated by silt-sized material, with modal sizes varying from 30–50 μm (Figure 3). In contrast, the eolian sand has a modal size of >100 μm and contains a small amount of fine silt (<20 μm). Within sections XS-A and XS-B, the mean grain sizes (M_z) of the loess and eolian sand fluctuate around 45 μm and 100 μm, respectively (Figure 2a). The M_z of the sand deposits in section KJ is slightly coarser than in sections XS-A and XS-B, which may be because the elevation of the site is similar to that of the upwind dune fields, which are relatively close to the section (Figure S1b). The M_z of sandy loess in the upper sections at these sites varies between values typical of eolian sand and loess in the sections, reflecting mixtures of sand-sized particles and loess silts (Figure 2a).

The strongly contrasting strata suggest that the deposition at the study sites was episodically dominated by distinctly different eolian dynamics and depositional settings. The loess deposits have grain-size distributions very similar to that of a typical loess sample from Lanzhou in the western CLP (Figure 3). Given windward nature of the loci where eolian deposits are preserved, the loess strata likely represent intervals dominated by a steppe environment, which can effectively protect deposited loess from subsequent eolian erosion (Sun & Ding, 1998). By contrast, the eolian sand is well-sorted, with grain-size distributions similar to that of a sand sample from mobile dunes, although the grain sizes are finer overall than the latter. At the XS site, sand deposition has been ascribed to the piling-up of sand due to the frequent occurrence of sand-laden storms across the adjacent deserts and to topographical effects, since *in situ* desertification and development of climbing dunes were ruled out (Qiang et al., 2010). Thus, compared to the interbedded loess, the sand deposits reflect either a reduced distance from sand sources to the sites and/or a strong wind regime (e.g., Ding et al., 1999); however, if so, this does not exclude the possibility that dune fields may have expanded into the vicinity of section KJ, given their similar altitude.

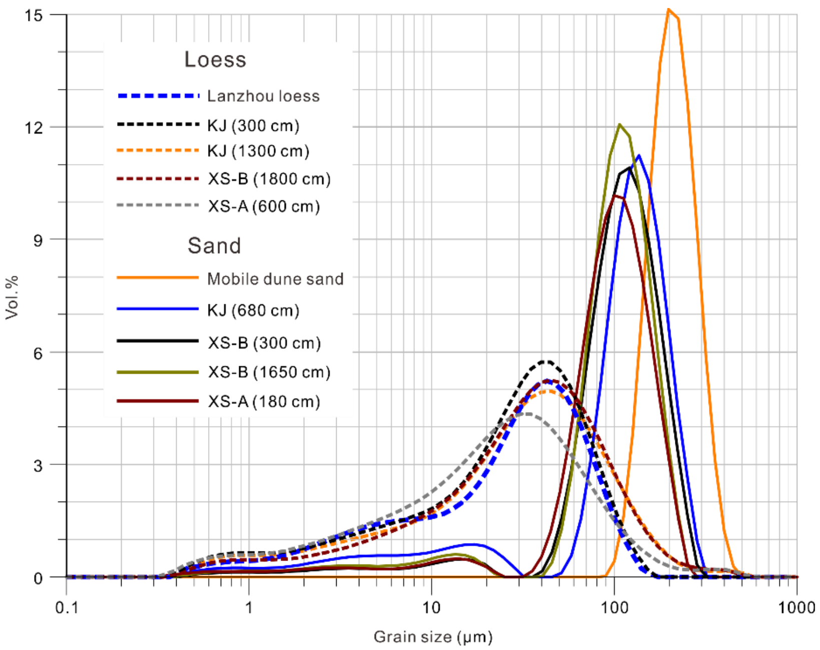

Figure 3. Contrasting grain-size distributions of representative samples of loess and eolian sand, compared with those of a sample of typical loess from Lanzhou and a sample of mobile dune. Samples depths are given in parentheses.

Abrupt increases in M_z occurred at the transitions from loess to eolian sand, i.e., roughly varying from 45 μm to 100 μm (Figure 2a); whereas from eolian sand to loess layers, the M_z decreases in a gradual manner. The abrupt grain-size changes are also clearly reflected in the distinctly different degree of compactness of loess and sand, as observed in the field. These point to sedimentation discontinuities at the loess to sand transitions. There are no signs of fluvial sediments and/or fluvial disturbance in the vicinity of the unconformities. Furthermore, the unconformity surfaces are easily identified in a large exposed area around the sampled sections (Figures 1b and 1c), and are almost flat, slightly inclined to northwest (Figure S2). The inclination is largely consistent with the direction of prevalent winds in seasons of intense eolian activity in the study areas (Sun et al., 2001; Qiang et al., 2014). Thus, we argue that the abrupt changes in grain size and alteration of stratigraphic units could represent unconformities induced by eolian erosion. There are at least four such stratigraphically identified hiatuses in the studied sections (Figure 2a). An apparent hiatus occurred from 42.5 to 25.4 ka in section XS-A, probably corresponding to one appearing at the depth of 390 cm in section XS-B, in light of an age of 14 ka from the middle of overlying sand layer. During this ~17-ka interval, airborne material may not have settled, and/or previously deposited loess may have been partially eroded by wind. We consider that the latter is very likely, taking into account the geomorphological signs and the drastic changes in grain size at the study sites described above. The exact timings of hiatuses in the lower parts of sections XS-B and KJ cannot be constrained due to the saturated luminescence signals meaning only minimum ages can be provided, and the large uncertainties inherent in the obtained dates.

Accounting for the locations of eolian deposits, their stratigraphic variability and the OSL/pIR IRSL dating, our results show that typical loess was previously deposited in the regions northwest to the CLP. The multiple erosional hiatuses uncovered at the transition from loess to eolian sand here strongly suggest that considerable amounts of pre-existing loess may have been significantly and episodically eroded by wind in these areas. As such, combined with evidence from desert marginal sections to the north of the CLP (Stevens et al., 2018), our chronostratigraphic evidence from sites west of the CLP lends further support to a proposed “eolian cannibalism” model of the evolution of the CLP (Kapp et al., 2015; Licht et al., 2016). Evidence from these CLP marginal areas points to previously more extensive loess cover that was subject to considerable erosion beyond the limits of the current CLP. Moreover, at section KJ, the upper loess/weak paleosol was truncated by fluvial process, and riverine deposits occurred between 19.3 and 17.4 ka. It is worthwhile noting also that besides eolain erosion, fluvial processes may have been another active agent for reworking of older loess (Licht et al., 2016). However, we note here that it is currently difficult to assess the volume of pre-existing loess in these CLP external sites that may have been removed, and therefore the degree to which these areas may once have made up an extended CLP, as envisaged by Kapp et al. (2015) and Licht et al. (2016). Nonetheless, our results show the important role that reworked loess on the margins of the CLP has in terms of dust sources to the CLP and beyond, as explored below.

3.2. The Effect of Wind Erosion of Pre-existing Loess on Dust Influx to the CLP

Dust from previously deposited loess upwind of the CLP can be entrained and then settled as components of CLP loess accumulation. However, examination of such a dynamic linkage requires a refined chronology of loess sequences. Recently, according to nine well-dated loess sections, Xu et al. (2018) suggested that there is an obvious seesaw pattern in dust accumulations during the past 20 ka across the CLP, and that the higher accumulation rates in the northwestern CLP during 20–15 ka may have been contributed to by loess reworking in upwind regions.

As for specific sites on the CLP, based on high stratigraphic resolution OSL dating, Stevens et al. (2016) measured changes in grain size and mass accumulation rate (MAR) since the last glacial at Xifeng (Figure 1 for location). This study showed that an increase in MAR between 39 and 32 ka at the section was not accompanied by an increase in grain size (Figure 2b), which is in conflict with the prevailing view that the two variables are highly correlated in loess (e.g., Vandenberghe et al., 1997). However, this contradiction and the enhanced dust MAR at Xifeng can potentially be explained by the occurrence of an erosional unconformity from 42.5 to 25.4 ka in section XS-A (Figure 2a): the increased MAR recorded at Xifeng could be a response to the deflation of pre-existing loess in upwind regions, followed by re-deposition downwind on the CLP, while the grain size was relatively invariant because the eroded and subsequently redeposited material itself consisted of loess. Indeed, our observation may explain general mismatches between grain size and dust MAR on sub-orbital timescales seen at a number of sites on the CLP (Stevens & Lu, 2009; Újvári et al., 2016). Similar unconformities in the lower parts of sections XS-B and KJ imply that wind erosion of previously deposited loess might occur within a number of intervals prior to the Late Pleistocene.

We suggest that the conversion of upwind loess deposits to dust sources must therefore be considered when using the loess deposits of the CLP to reflect large-scale patterns of Asian dust transport and deposition. For example, dust MAR estimated from loess deposits, some of which have been used to help simulate past relative dust loading (e.g., Albani et al., 2015), may be enhanced at the central CLP sites by this process, potentially leading to overestimates of dust source activity in regions further upwind of the Loess Plateau. Furthermore, the input of homogeneous, silt-sized particles of pre-existing loess from upwind areas would bias the grain size of corresponding loess deposits on the CLP to be less variable or even to be overall smaller compared to their adjacent strata, as grain size is a function not only of wind speed but also source sediment characteristics and distance to source (Újvári et al., 2016). In this case, it is unrealistic to simply explain reductions in grain size as indicating stable or weaker wind regimes, or even strengthened summer monsoonal circulation over the CLP. Rather, intensive eolian activity may have been occurring in upwind areas at those times.

3.3. The Role of Proximal Desert Evolution on Dust Dynamics

Given that sand-sized particles are transported for short ranges even under strong wind conditions (Pye, 1987), the homogenous, well-sorted sand deposits at the study sites primarily reflect expansions of proximal deserts, e.g., the Tengger Desert and the Mugetan Sandy Land (Figure S1). As shown in section XS-A, the recent expansion of the Tengger Desert occurred during 25.4–12.2 ka, or somewhat earlier, which might be supported by the presence of sand deposition in section XS-B, dated as old as 14.0 ka (Figure 2a). Multiple episodes of expansions of proximal deserts are also indicated by the sand deposition in sections KJ and XS-B.

The grain-size variability along the profiles can further clarify the spatial variation of proximal deserts, since the advance-retreat cycles of the deserts play an important role in defining the grain size of loess deposition (Ding et al., 1999). Beneath the sandy loess/paleosol in the upper parts of the sections, the alternating loess and sand units exhibit contrasting M_z values, with relatively uniform values within their respective units (Figure 2a). In addition, in sections XS-B and KJ, the typical loess deposited above sand layers has grain-size distributions very similar to the older loess underlying the sand layers (Figures 2a and 3). These observations imply that when the typical loess is deposited at the sites, the active, previously expanded proximal deserts, represented by the layers of well-sorted sand deposition, may have greatly contracted and/or even been completely fixed following the initiation of loess accumulation. According to investigations on grain sizes of coeval loess deposits along a transection from north to south across the CLP, Ding et al. (1999) proposed that sand content (>63 μm proportion) of loess in the marginal areas of the CLP could monitor changes in the extent of proximal deserts over the past. Taking section XS-A as an example (Figure 2a), during 66.0–42.5 ka the lower sand content (<30%) of the loess suggests a possible distance of ~100 km to the desert at that time, in light of the model proposed by Ding et al. (1999). This is much larger than the modern distance of ~20 km. Similar situations are recorded by sections KJ and XS-B, suggesting a dynamic desert environment generally. In this respect, our results are in contrast to the conclusion that the Tengger Desert has been a relatively constant active sandy desert environment since 0.68 Ma (Li et al., 2014). In fact, a paleo-megalake in the desert occurred from 42 to 18 ^{14}C ka B.P. (Zhang et al., 2002), despite the radiocarbon dates possibly being underestimated (e.g., Madsen et al., 2014). Core sediments from the Badain Jaran Desert also show that from 0.65 to 0.45 Ma a large lake occupied the desert center (Wang et al., 2015). Furthermore, episodic expansions of the Mu Us Sandy Land during the Marine Isotope Stages (MIS) 2–4 and 6 are illustrated by either erosional hiatuses or sand deposition recorded in the well-dated Jingbian section (Stevens et al., 2018). Although the available evidence cannot depict the detailed history of proximal deserts, it is plausible that the region may have experienced drastic hydroclimatic changes, which dramatically affect dust emission and transport, and hence the nature of eolian deposits downwind, as observed at the study sites.

Given the intermediate M_z of sandy loess/paleosol, compared to lower loess and sand in section XS-A (Figure 2a), the Tengger Desert may not have retreated as drastically after the recent phase of expansion at 25.4–12.2 ka as occurred previously, when the typical loess units were deposited. Although the weakly-developed paleosols perhaps depict a relatively warm and wet climate during some intervals of the Holocene (Figure 2a), the desert may still have had areas of activated eolian sand sufficient for the sandy loess to be deposited throughout the Late Glacial and the Holocene. In section KJ, the sandy loess/paleosol occurred since 17.4 ka, and the M_z values are intermediate and less variable until the present. These suggest that the Mugetan Sandy Land could already have existed at this time and may even have been very close to its modern position, likely reflecting proximal desert expansion during Last Glacial Maximum (LGM) in this area. In fact, the proximal deserts in northern China had expanded greatly during the LGM, and the Tengger Desert and the Gonghe Sandy Land areas have been estimated to be greater by ~30% and 20% of their modern sizes, respectively (Lu et al., 2013). Such large-scale desert expansions were probably driven by an abrupt shift to an extremely cold and dry climate during the LGM (Stevens et al., 2013).

Given a material linkage between source and sink, it is expected that this large-scale desert expansion would be tracked in loess records downwind. In fact, an increase in the accumulation rate of loess deposits downwind occurred at ~20 ka, as evidenced by a ~2.5-m-thick unit in the Beiguoyuan section on the northern CLP; moreover, the sediment source of this unit shifted abruptly to a local source from the previous well-mixed and recycled remote sources (Stevens et al., 2013). A high MAR of loess deposition during the LGM appears to be observed in large regions, even on the Serbian Titel Loess Plateau (Stevens et al., 2016; Perić et al., 2019). Indeed, based on closely-spaced OSL dates, the loess MARs estimated at eight sites on the CLP were distinctly higher from ~23 to 19 ka (Kang et al., 2015). Under colder and drier climatic conditions during the LGM, enhanced dune activity resulted in erosion of underlying loess strata and hence hiatuses in marginal loess sections (Stevens et al., 2013, 2018). Expanded dune fields and entrained pre-existing loess materials upwind of the CLP would have led to MAR increases together over the CLP. In this regard, the high loess MARs on the CLP during the LGM might not necessarily represent greater wind strength (e.g., Kang et al., 2015) or enhanced silt production through grain to grain impacts and abrasion in migrating dune systems (e.g., Lancaster, 2020), but rather erosion of pre-existing upwind loess and deflation of widespread silt deposits stored in deserts, alluvial fans and river floodplains (e.g., Derbyshire et al., 1998). However, higher wind speeds could still be one of the crucial factors for sand movement in desert environments and dune movement would still be required to erode and mobilize the silt particles locked up in loess deposits upwind of the CLP. Similarly, such a causal linkage between expansions of proximal deserts and loess deposition has to be considered for some intervals prior to the LGM, as suggested by the stratigraphically lower sand layers at the study sites, but assessment on this requires refined chronology of CLP marginal sites around the CLP and desert margins.

4. Conclusions

The alternating strata of loess and well-sorted sand at the study sites show that typical loess deposits have been distributed in upwind areas of the present CLP. The pre-existing loess was eroded by winds capable of moving sands within some intervals of the Quaternary and episodically transformed to an additional dust source for loess accumulation on the CLP. The entrained loess materials will obviously result in changes in grain size and MAR of CLP loess sequences. This process provides a reasonable explanation for the recently observed contradictions between the two parameters in the late glacial loess deposits on the central CLP. Furthermore, the variable extent of proximal deserts also plays an important role in dust emission and transport, giving rise to major changes in dust accumulation rates on the CLP, especially during the LGM expansion of proximal deserts. Our results firstly provide stratigraphic evidence supporting at least some cannibalization of previously deposited loess (Kapp et al., 2015) outside of the modern CLP, and highlight dynamic dust activity in upwind regions that apparently complicate climatic interpretations from Chinese loess sequences. Despite of some dating uncertainties presented here, the significantly contrasting stratigraphic variability strongly suggests that the history of dust activity in upwind regions is of particular significance for thorough understanding of climate and dust changes recorded by Quaternary loess deposits. Thus, more well-dated eolian sequences from broad upwind areas of the CLP, in combination with other types of environmental records, would be important to elucidate these dust processes, including changes in desert environment and their potential forcing mechanisms.

Acknowledgements

This research was supported by the National Science Foundation of China (grants 41671190) and the National Key R&D Program of China (grant 2017YFA0603402). The grain size data are available at the Figshare repository: https://doi.org/10.6084/m9.figshare.12301283.

References

Aitken, M. J. (1998). *An Introduction to Optical Dating*. Oxford, UK: Oxford University Press.

Albani, S., Mahowald, N. M., Winckler, G., Anderson, R. F., Bradtmiller, L. I., Delmonte, B., François, R., Goman, M., Heavens, N. G., Hesse, P. P., Hovan, S. A., Kohfeld, K. E., Lu, H., Maggi, V., Mason, J. A., Mayewski, P. A., McGee, D., Miao, X., Otto-Bliesner, B. L., Perry, A. T., Pourmand, A., Roberts, H. M., Rosenbloom, N., Stevens, T., & Sun, J. (2015). Twelve thousand years of dust: the

Holocene global dust cycle constrained by natural archives. *Climate of the Past, 11*(6), 869–903, doi:1 0.5194/cp-11-869-2015.

Biscaye, P. E., Grousset, F. E., Revel, M., Van der Gaast, S., Zielinski, A., Vaars, A., & Kukla, G. (1997). Asian provenance of glacial dust (stage 2) in the GISP2 ice core, Summit, Greenland. *Journal of Geophysical Research, 102*(C12), 26675–26781, doi:10.1029/97JC01249.

Buylaert, J. P., Jain, M., Murray, A. S., Thomsen, K. J., Thiel, C., & Sohbati, R. (2012). A robust feldspar luminescence dating method for middle and late Pleistocene sediments. *Boreas, 41*(3), 435–451, doi: 10.1111/j.1502-3885.2012.00248.x.

Buylaert, J. P., Yeo, E. Y., Thiel, C., Yi, S. W., Stevens, T., Thompson, W., Frechen, M., Murray, A. S., & Lu, H. Y. (2015). A detailed post-IR IRSL chronology for the last interglacial soil at the Jingbian loess site (northern China), *Quaternary Geochronology, 30*, 194–199, doi: 10.1016/j.quageo.2015.02.022.

Derbyshire, E., Meng, X. M., & Kemp, R. A. (1998). Provenance, transport and characteristics of modern Aeolian dust in western Gansu Province, China, and interpretation of the Quaternary loess record. *Journal of Arid Environments, 39*(3), 497–516, doi:10.1006/jare.1997.0369.

Ding, Z. L., Sun, J. M., Rutter, N. W., Rokosh, D., & Liu, T. S. (1999). Changes in sand content of loess deposits along a north-south transect of the Chinese Loess Plateau and implications for desert variations for desert variations. *Quaternary Research, 52*(1), 56–62, doi:10.1006/qres.1999.2045.

Guérin, G., Mercier, N., & Adamiec, G. (2011). Dose-rate conversion factors: update.

Ancient TL, 29, 5–8.

Guo, Z. T., Ruddiman, W. F., Hao, Q. Z., Wu, H. B., Qiao, Y. S., Zhu, R. X., Peng, S. Z., Wei, J. J., Yuan, B. Y., & Liu, T. S. (2002). Onset of Asian desertification by 22 Myr ago inferred from loess deposits in China. *Nature, 416*(6877), 159–163, doi:10.1038/416159a.

Hovan, S. A., Rea, D. K., Pisias, N. G., & Shackleton, N. J. (1989). A direct link between the China loess and marine $\delta^{18}O$ records: Aeolian flux to the north Pacific. *Nature, 340*(6231), 296–298, doi: 10.1038/340296a0.

Huntley, D. J., & Hancock, R. G. V. (2001). The Rb contents of the K-feldspars being measured in optical dating. *Ancient TL, 19,* 43–46.

Huntley, D. J., & Baril, M. R. (1997). The K content of the K-feldspars being measured in optical dating or in thermoluminescence dating. *Ancient TL, 15,* 11–13.

Kang, S. G., Roberts, H. M., Wang, X. L., An, Z. S., & Wang, M. (2015). Mass accumulation rate changes in Chinese loess during MIS2, and asynchrony with records from Greenland ice cores and North Pacific Ocean sediments during the Last Glacial Maximum. *Aeolian Research, 19,* 251–258, doi:10.1016/j.aeolia.2015.05.005.

Kapp, P., Pullen, A., Pelletier, J. D., Russell, J., Goodman, P., & Cai, F. L. (2015). From dust to dust: Quaternary wind erosion of the Mu Us Desert and Loess Plateau, China. *Geology, 43*(9)*,* 835–838, doi: 10.1130/G36724.1.

Lancaster, N. (2020). On the formation of desert loess, *Quaternary Research,* doi.org/10.1017/qua.2020.33.

Li, Z. J., Sun, D. H., Chen, F. H., Wang, F., Zhang, Y. B., Guo, F., Wang, X., & Li, B. F. (2014). Chronology and paleoenvironmental records of a drill core in the central Tengger Desert of China. *Quaternary Science Reviews, 85,* 85–98, doi:10.1016/j.quascirev.2013.12.003.

Licht, A., van Cappelle, M., Abels, H. A., Ladant, J. B., Trabucho-Alexandre, J., France-Lanord, C., Donnadieu, Y., Vandenberghe, J., Rigaudier, T., Lécuyer, C., Terry Jr, D. O., Adriaens, R., Boura, A., Guo, Z., Soe, A. N., Quade, J., Dupont-Nivet, G., & Jean-Jacques, J. (2014). Asian monsoon in a late Eocene greenhouse world. *Nature, 513*(7519)*,* 501–506, doi:10.1038/nature13704.

Licht, A., Pullen, A., Kapp, P., Abell, J., & Giesler, N. (2016). Eolian cannibalism: Reworked loess and fluvial sediment as the main sources of the Chinese Loess Plateau. *Geological Society of America Bulletin, 128*(5-6), 944–956, doi: 10.1130/B31375.1.

Liu, T. S., & Ding, Z. L. (1998). Chinese loess and the paleomonsoon. *Annual Review of Earth and Planetary Sciences, 26,* 111–145, doi:10.1146/annurev.earth.26.1.111.

Lu, H. Y., Yi, S. W., Xu, Z. W., Zhou, Y. L., Zeng, L., Zhu, F. Y., Feng, H., Dong, L. N., Zhou, H. X., Yu, K. F., Mason, J., Wang, X. Y., Chen, Y. Y., Lu, Q., Wu, B., Dong, Z. B., Qu, J. J., Wang, X. M., & Guo, Z. T. (2013). Chinese deserts and sand fields in Last Glacial Maximum and Holocene Optimum. *Chinese Science Bulletin, 58*(23), 2775–2783, doi:10.1007/s11434-013-5919-7.

Madsen, D. B., Lai, Z. P., Sun, Y. J., Rhode, D., Liu, X. J., & Brantingham, P. J. (2014). Late Quaternary Qaidam lake histories and implications for an MIS 3 “Greatest

Lakes" period in northwest China. *Journal of Paleolimnology, 51*(2), 161-177, doi:10.1007/s10933-012-9662-x.

Perić, Z., Adolphi, E. L., Stevens, T., Újvári, G., Zeeden, C., Buylaert, J.-P., Marković, S. B., Hambach, U., Fischer, P., Schmidt, C., Schulte, P., Lu, H. Y., Yi, S. W., Lehmkuhl, F., Oberht, I., Veres, D., Thiel, C., Frechen, M., Jain, M., Vött, A., Zöller, L., & Gavrilov, M. B. (2019). Quartz OSL dating of late quaternary Chinese and Serbian loess: A cross Eurasian comparison of dust mass accumulation rates. *Quaternary International, 502,* 30–44, doi:10.1016/j.quaint.2018.01.010.

Prescott, J. R., & Hutton, J. T. (1994). Cosmic ray contributions to dose rates for luminescence and ESR dating: large depths and long-term time variations. *Radiation Measurements, 23,* 497–500, doi:10.1016/1350-4487(94)90086-8.

Pye, K. (1987). *Aeolian Dust and Dust Deposits*. London: Academic Press.

Qiang, M. R., Chen, F. H., Wang, Z. T., Niu, G. M., & Song, L. (2010). Aeolian deposits at the southeastern margin of the Tengger Desert (China): Implications for surface wind strength in the Asian dust source area over the past 20,000 years. *Palaeogeography Palaeoclimatology Palaeoecology, 286*(1)*,* 66–80, doi:10.1016/j.palaeo.2009.12.005.

Qiang, M. R., Liu, Y. Y., Jin, Y. X., Song, L., Huang, X. T., & Chen, F. H. (2014). Holocene record of eolian activity from Genggahai Lake, northeastern Qinghai-Tibetan Plateau, China. *Geophysical Research Letters, 41*(2)*,* 589–595, doi: 10.1002/2013GL058806.

Rea, D. K. (1994). The paleoclimatic record provided by eolian deposition in the deep sea: The geologic history of wind. *Reviews of Geophysics, 32*(2), 159–195, doi: 10.1029/93RG03257.

Shao, Y. P., Wyrwoll, K. H., Chappell, A., Huang, J. P., Lin, Z. H., McTainsh, G. H., Mikami, M., Tanaka, T. Y., Wang, X. L., & Yoon, S. (2011). Dust cycle: An emerging core theme in Earth system science. *Aeolian Research, 2*(4), 181–204, doi:10.1016/j.aeolia.2011.02.001.

Stevens, T., Adamiec, G., Bird, A. F., & Lu, H. Y. (2013). An abrupt shift in dust source on the Chinese Loess Plateau revealed through high sampling resolution OSL dating. *Quaternary Science Reviews, 82,* 121–132, doi:10.1016/j.quascirev.2013.10.014.

Stevens, T., Armiitage, S. J., Lu, H. Y., & Thomas, D. S. G. (2006). Sedimentation and diagenesis of Chinese loess: Implication for the preservation of continuous, high-resolution climate records. *Geology, 34*(10), 849–852, doi:10.1130/G22472.1.

Stevens, T., Buylaert, J. P., Lu, H. Y., Thiel, C., Murry, A., Frechen, M., Yi, S. W., & Zeng, L. (2016). Mass accumulation rate and monsoon records from Xifeng, Chinese Loess Plateau, based on a luminescence age model. *Journal of Quaternary Science, 31*(4), 391–405, doi: 10.1002/jqs.2848.

Stevens, T., Buylaert, J. P., Thiel, C., Újvári, G., Yi, S. W., Murray, A. S., Frechen, M., & Lu, H. Y. (2018). Ice-volume-forced erosion of the Chinese Loess Plateau global Quaternary stratotype site. *Nature Communications, 9*(1), 983–994, doi:10.1038/s41467-018-03329-2.

Stevens, T., & Lu, H. Y. (2009). Optically stimulated luminescence dating as a tool for calculating sedimentation rates in Chinese loess: comparisons with grain-size records. *Sedimentology, 56*(4)*,* 911–934, doi: 10.1111/j.1365-3091.2008.01004.x.

Sun, J. M., & Ding, Z. L. (1998). Deposits and soils of the past 130,000 years at the desert-loess transition in northern China. *Quaternary Research, 50*(2)*,* 148–156, doi:10.1006/qres.1998.1989.

Sun, J. M., Zhang, M. Y., & Liu, T. S. (2001). Spatial and temporal characteristics of dust storms in China and its surrounding regions, 1960-1999: Relation to source area and climate. *Journal of Geophysical Research, 106*(D10)*,* 10325–10333, doi:10.1029/2000JD900665.

Sun, Y. B., Clemens, S. C., Morrill, C., Lin, X. P., Wang, X. L., & An, Z. S. (2012). Influence of Atlantic meridional overturning circulation on the East Asian winter monsoon. *Nature Geoscience, 5*(1)*,* 46–49, doi:10.1038/ngeo1326.

Uno, I., Eguchi, K., Yumimoto, K., Takermura, T., Shimizu, A., Uematsu, M., Liu, Z., Wang, Z., Hara, Y., & Sugimoto, N. (2009). Asian dust transported one full circuit around the globe. *Nature Geoscience, 2*(8), 557–560, doi:10.1038/ngeo583.

Újvári, G., Kok, J. F., Varga, G., & Kovács, J. (2016). The physics of wind-blown loess: Implications for grain size proxy interpretations in Quaternary paleoclimate studies. *Earth-Science Reviews, 154,* 247–278, doi:10.1016/j.earscirev.2016.01.006

Vandenberghe, J., An, Z. S., Nugteren, G., Lu, H. Y., & Van Huissteden, K. (1997). New absolute time scale for the Quaternary climate in the Chinese Loess region by grain-size analysis. *Geology, 25*(1)*,* 35–38, doi:10.1130/0091-

7613(1997)025<0035:NATSFT>2.3.CO;2.

Wang, F., Sun, D. H., Chen, F. H., Bloemendal, J., Guo, F., Li, Z. J., Zhang, Y. B., Li, B. F., & Wang, X. (2015). Formation and evolution of the Badain Jaran Desert, North China, as revealed by a drill core from the desert centre by geological survey. *Palaeogeography Palaeoclimatology Palaeoecology, 426,* 139–158, doi:10.1016/j.palaeo.2015.03.011.

Xu, Z.W., Stevens, T., Yi, S.W., Mason, J.A., & Lu, H.Y. (2018). Seesaw pattern in dust accumulation on the Chinese Loess Plateau forced by late glacial shifts in the East Asian monsoon. *Geology, 46*(10)*,* 871–874, doi:10.1130/G45105.1.

Yi, S.W., Li, X. S., Han, Z. Y., Lu, H. Y., Liu, J. F., & Wu, J. (2018). High resolution luminescence chronology for Xiashu Loess deposits of Southeastern China. *Journal of Asian Earth Science, 155,* 188–197, doi:10.1016/j.jseaes.2017.11.027.

Zhang, H. C., Wünnemann, B., Ma, Y. Z., Peng, J. L., Pachur, H. J., Li, J. J., Qi, Y., Chen, G. J., Fang, H. B., & Feng, Z. D. (2002). Lake level and climate changes between 42,000 and 18,000 ^{14}C yr B.P. in the Tengger Desert, northwestern China. *Quaternary Research, 58*(1)*,* 62–72, doi:10.1006/qres.2002.2357.

AGU PUBLICATIONS

Geophysical Research Letters

Supporting Information for

Late Quaternary Dust, Loess and Desert Dynamics in Upwind Areas of the Chinese Loess Plateau

Mingrui Qiang[1,2], Thomas Stevens[3], Guoqiang Li[2], Ling Hu[2], Xiaowei Wang[2], Wenzhe Lang[2], and Jie Chen[1]

[1] School of Geography, South China Normal University, Guangzhou 510631, China, [2] MOE Key Laboratory of Western China's Environmental Systems, Lanzhou University, Lanzhou 730000, China, [3] Department of Earth Sciences, Uppsala University, Villavägen 16, Uppsala 75236, SwedenInstitutional affiliations]

Contents of this file

Text S1 to S2

Figures S1 to S4

Tables S1

Introduction

The auxiliary material contains additional information supporting the manuscript, including detailed physical environments of the study sites, a close-up view of stratigraphic variability of section XS-B emphasizing wind erosion surfaces, and the methodology of K-feldspar post-IR

Infra-Red Stimulated Luminescence (IRSL) dating and the luminescence results, as well the method of grain size measurement.

Text S1.

Grain Size Measurement

Sediment grain-size distributions were measured using a laser particle analyzer (Malvern Mastersizer 2000), after removing organic matter and carbonate by H_2O_2 and HCl followed by dispersion with $(NaPO_3)_6$. The measurement range is 0.02–2000 μm.

Text S2.

K-feldspar post-IR Infra-Red Stimulated Luminescence (IRSL) Dating

K-feldspar pIRIR dating results, as well as detail from previous quartz optically stimulated luminescence (OSL) dating and other relevant data are shown in Table S1. In addition to new pIRIR ages we also quote the previously published quartz OSL ages from section XS-A (Qiang et al., 2010), as well as a new single quartz OSL age from XS-A using the same methods. These OSL ages were used to reconstruct changes in wind strength over the past 20 ka. Detailed analytical information was given by Qiang et al. (2010).

In this study, luminescence dating samples were measured using a K-feldspar pIRIR dating protocol. Sample preparation followed the methods described by Aitken (1998). All laboratory processing, including sample preparation and luminescence measurements, was carried out in a darkroom under subdued red light in the Luminescence Laboratory at Lanzhou University, China. All samples were treated with 10% HCl and 20% H_2O_2 to remove carbonate and organic matter, respectively, and then wet sieved to extract sediments of grain sizes of 63/90–125 μm. Heavy liquid with a density of 2.58 g cm^{-3} was used to separate the K-feldspar fraction of each sample. The K-feldspar grains were treated with 10% HF for 40 min to remove the outer layer irradiated by alpha particles. All samples were further treated with 1 mol l^{-1} HCl for 10 min to remove fluorides produced during the HF etching. K-feldspar IRSL signal was measured using an automated Risø TL/OSL-DA-20 reader. Laboratory irradiation was carried out using $^{90}Sr/^{90}Y$ sources mounted within the reader. The IRSL signal was detected using a photomultiplier tube with the IRSL passing through BG-39 and Coring-759 filters.

A prior IR stimulation temperature plateau test (Buylaert et al., 2012; Yi et al., 2018) was conducted on the sand sample XS-A-07 to check the stability of the pIRIR signal. The pIRIR De values were obtained in 6 groups of aliquots with different prior IR stimulation temperature from 50ºC to 270ºC measured at 30ºC intervals (three aliquots each group). As illustrated in Figure S3, the pIRIR De have not shown an obvious trend with prior IR stimulation temperature increasing from 50ºC to 230ºC, indicating the stability of pIRIR signal. A prior IR stimulation temperature of 50ºC is used in pIRIR dating protocol.

A dose recovery test was conducted on sunlight bleached samples XS-B-01 (sand) and XS01-A-07 (loess) to check the suitability of the chosen pIRIR dating protocol. Seven aliquots of each sample were bleached under sunlight for 28 h in March in Lanzhou, China. The residual dose of each sample was measured by using the pIRIR dating protocol and then a given dose of the 59.4 Gy was added to four bleached aliquots of sample XS-B-01 and a given dose of 297 Gy were added to four bleached aliquots of sample XS-A-07. The pIRIR De of these two samples are then measured by using the pIRIR dating protocol. The measured/given dose ratio of the K-feldspar sample XS-B-01 and XS-A-07 is 0.91±0.01 and 0.89±0.02, respectively. If the measured residual doses of 4.63 ±0.13 Gy and 7.85±0.40 Gy were subtracted from the corresponding measured dose, the measured/given dose ratios are 0.83±0.01 and 0.86±0.02. Given the uncertainty of the measurement of the residual dose, these measured/given dose ratios are considered acceptable for the pIRIR dating protocol.

The environmental dose rate was calculated from the measurements of radioactive element concentrations in the sample with a small contribution from cosmic rays. For all samples, the concentrations of uranium (U), thorium (Th) and potassium (K) were determined using neutron activation analysis (NAA). All results were converted to beta and gamma dose rates using the conversion factors by Guérin et al. (2011). The dose rate from cosmic rays was calculated from the sample burial depth and the altitude of the section (Prescott & Hutton, 1994). The internal dose rate of K-feldspar grains was calculated with a K content of 12.5%±0.5% (Huntley & Baril, 1997) and a Rb content of 400±100 ppm (Huntley & Hancock, 2001). The measured in situ water content was used to calculate ages for all loess/sand samples. Fifty percent of individual measured value was taken as water content errors.

The decay curves and growth curves for coarse-grained K-feldspar sample XS-B-02 are illustrated in Figure S4. The initial $pIRIR_{290}$ signal shows much higher values compared to the

IR_{50} signal. The growth curve for the sample can be readily fitted using a single saturation exponential function. The $2D_0$ (luminescence saturation parameter) calculated from the growth curves of $pIRIR_{290}$ signal of the sample is 694±37 Gy, respectively, indicating an upper limit of 700 Gy of $pIRIR_{290}$ signal for samples from this region. Similarly, the $pIRIR_{290}$ signal has shown a similar but slightly higher saturation dose of 800 Gy for loess samples from the Jingbian desert marginal site (Stevens et al., 2018). As a result, the $pIRIR_{290}$ D_e values of samples less than 700 Gy are accepted as reliable D_e values (Table S1), while the $pIRIR_{290}$ D_es of samples that are larger than 700 Gy are considered as minimum De estimaets as a result of the saturation of the $pIRIR_{290}$ signal of these samples.

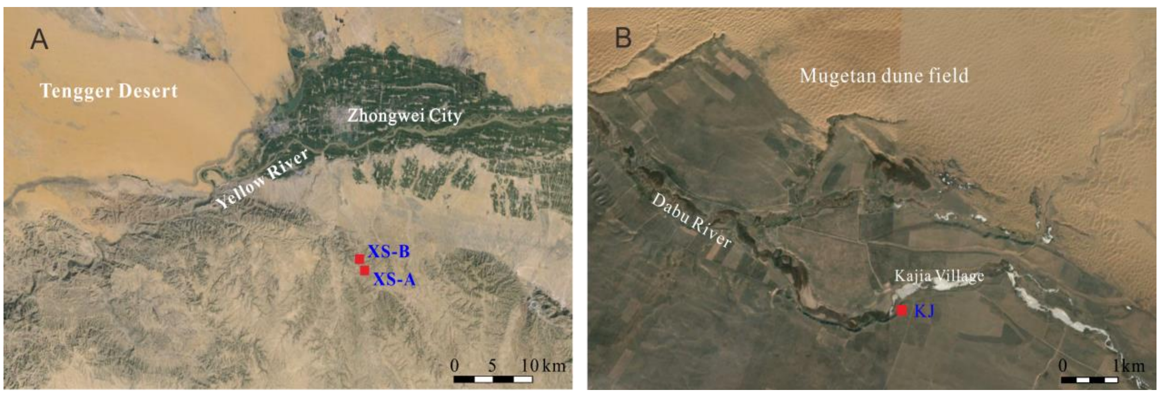

Figure S1. Close-up view (Google EarthTM) of the physical environments surrounding sections XS-A/B (a) and KJ (b).

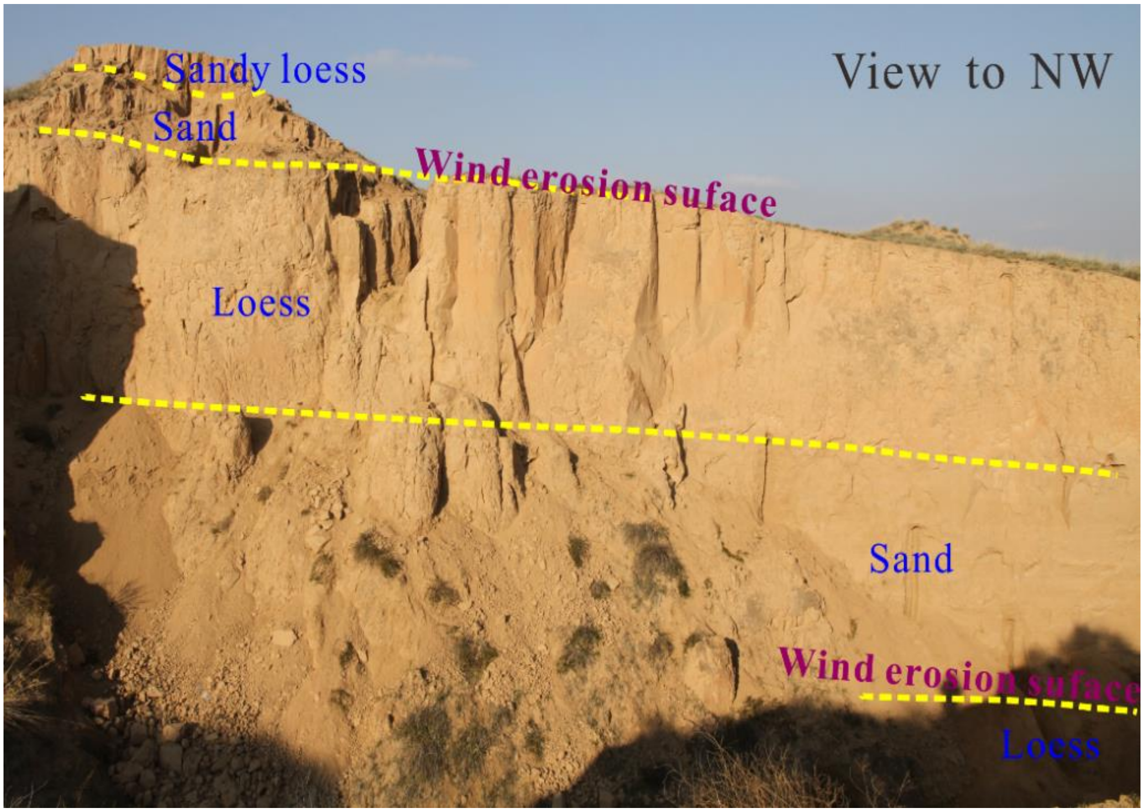

Figure S2. Photograph of section XS-B. The lithostratigraphic units are delineated. Flat surfaces, clearly identified at the transitions from loess to sand deposition in the section, are characterized by abrupt alternation of sediment, no signs of fluvial activity, and inclination to NW that is in agreement with the direction of prevalent winds in winter and spring seasons, indicating erosional hiatuses by wind.

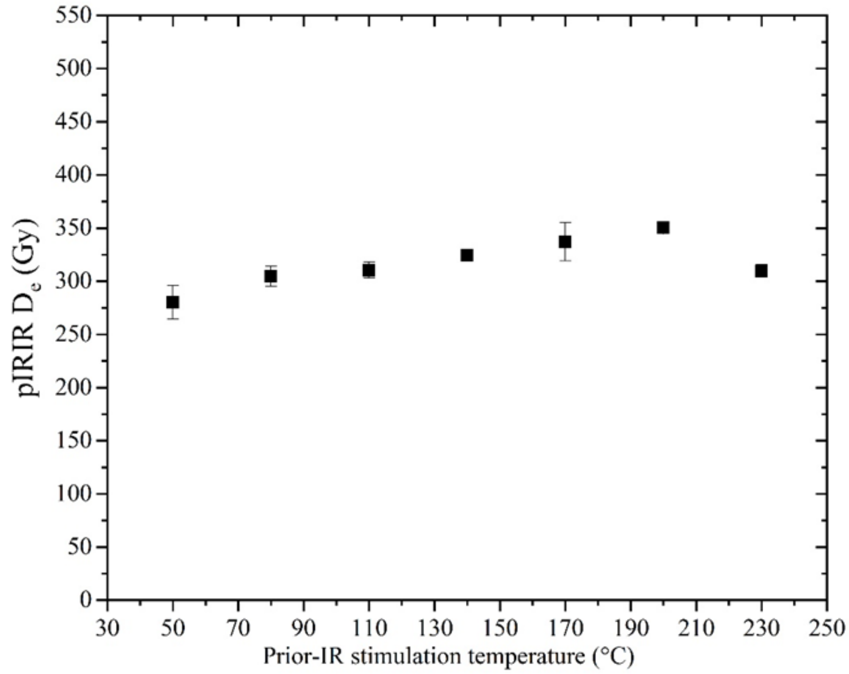

Figure S3. Plot of pIRIR De to prior IR stimulation temperature for K-feldsapr sample XS-A-07.

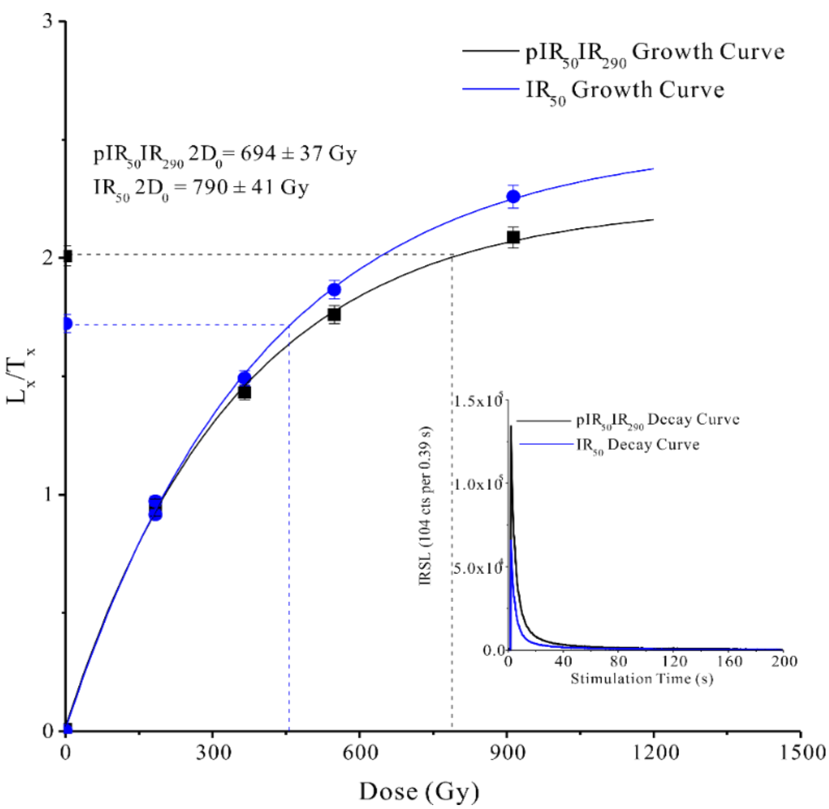

Figure S4. Decay curves and growth curves of K-feldspar sample XS-B-02.

Section	Sample No.	Sediment type	Depth (cm)	Mineral	Grain size (μm)	Water content (%) [b]	U (ppm)	Th (ppm)	K (%)	Dose rate (Gy/ka)	D_e (Gy)	Age (ka)	Reference
XS-A	XS-A-01	Loess	46	Quartz	63−150	2.1	2.69±0.10	9.59±0.25	1.64±0.12	2.97±0.15	21.4±1.2	7.2±0.6	Qiang et al., 2010
	XS-A-02	Loess	100	Quartz	63−150	3.5	2.05±0.10	7.58±0.25	1.75±0.11	2.76±0.16	29.3±4.9	10.6±1.8	Qiang et al., 2010
	XS-A-03	Eolian sand	170	Quartz	63−150	1.3	1.56±0.10	7.02±0.25	1.97±0.11	2.90±0.15	35.4±2.8	12.2±1.2	Qiang et al., 2010
	XS-A-04	Eolian sand	480	Quartz	63−150	1.6	1.51±0.10	7.50±0.25	1.73±0.14	2.64±0.15	67.1±4.4	25.4±2.2	Unpublished data
	XS-A-05	Loess	510	Quartz	63−150	5.8	2.87±0.10	13.5±0.28	1.80±0.12	3.31±0.16	140.8±6.2	42.5±2.8	Qiang et al., 2010
	XS-A-06	Loess	1080	Quartz	63−150	5.3	2.45±0.11	11.3±0.26	1.86±0.12	3.13±0.15	172±6.9	55.0±3.5	Qiang et al., 2010
	XS-A-07	Loess	1250	K-Feldspar	90−125	2.7	2.82±0.04	10.4±0.03	1.86±0.03	4.37±0.30	290±10	66.0±5.0	This study
XS-B	XS-B-01	Eolian sand	350	K-Feldspar	90−125	1.3	2.22±0.04	8.32±0.03	1.69±0.03	4.10±0.30	59.0±1.00	14.0±1.0	This study
	XS-B-02	Loess	530	K-Feldspar	90−125	0.8	2.72±0.04	10.5±0.03	1.87±0.03	4.57±0.30	808±71	177±19 [a]	This study
	XS-B-03	Loess	900	K-Feldspar	60−125	1.9	2.45±0.10	9.09±0.26	1.85±0.06	3.67±0.10	796±68	217±19 [a]	This study
	XS-B-04	Eolian sand	950	K-Feldspar	90−125	0.7	2.17±0.04	8.72±0.03	1.70±0.03	4.19±0.30	844±72	201±22 [a]	This study
	XS-B-05	Eolian sand	1635	K-Feldspar	90−125	0.9	1.75±0.05	7.41±0.03	1.96±0.03	4.19±0.30	1004±89	240±27 [a]	This study
	XS-B-06	Eolian sand	1750	K-Feldspar	60−125	2.1	2.07±0.08	7.10±0.24	1.78±0.06	3.42±0.09	789±105	230±20 [a]	This study
	XS-B-07	Loess	1795	K-Feldspar	60−125	4.8	2.76±0.10	10.3±0.28	1.80±0.05	3.71±0.09	693±69	187±19 [a]	This study
	XS-B-08	Loess	1990	K-Feldspar	90−125	1.9	3.12±0.04	10.7±0.03	1.89±0.03	4.64±0.30	826±82	178±21 [a]	This study
KJ	KJ-01	Fluvial sand	150	K-Feldspar	90−125	5.3	2.33±0.09	8.10±0.24	1.76±0.05	3.31±0.10	57.6±2.8	17.4±1.0	This study
	KJ-02	Loess/Paleosol	260	K-Feldspar	90−125	4.2	1.50±0.07	7.42±0.24	1.58±0.05	2.94±0.10	56.8±1.2	19.3±0.8	This study
	KJ-03	Eolian sand	680	K-Feldspar	60-125	1.4	1.57±0.07	9.38±0.27	1.33±0.05	3.31±0.09	785±40	237±14 [a]	This study
	KJ-04	Eolian sand	880	K-Feldspar	60−125	2.3	1.51±0.07	7.20±0.23	1.39±0.05	2.92±0.08	802±452	274±17 [a]	This study
	KJ-05	Loess	920	K-Feldspar	60−125	5.1	2.08±0.09	8.40±0.25	1.62±0.05	3.27±0.09	883±67	270±21 [a]	This study
	KJ-06	Loess	1880	K-Feldspar	90−125	4.8	2.29±0.04	11.4±0.03	1.92±0.03	4.52±0.30	901±72	199±21 [a]	This study

[a] Estimated as minimum ages.

[b] Errors: fifty percent of the measured value.

Table S1. Luminescence dating results of the eolian deposits